# Electron-Ion Transport in $ZrO_2$-$Y_2O_3$-$CeO_2$ Ceramics

C.M. CHUN,* J.D. MUMFORD, J. PATEL & T.A. RAMANARAYANAN[†]

*ExxonMobil Research and Engineering Company, Corporate Strategic Research, Annandale, NJ 08801, USA*

**Abstract.** Simultaneous conduction of oxide ions and electrons in solid ceramic systems provides the capability for oxygen transport under a concentration gradient without the need for an externally applied electric field. In the present study, ionic transference numbers have been measured in the $ZrO_2$-5.8%$Y_2O_3$-10%$CeO_2$ system by open circuit Emf measurements involving different metal/metal oxide electrodes. In order to correlate the ionic transference number with grain size, high-density ceramic discs of different grain sizes (50 nm–5 $\mu$m) were prepared by sintering pressed powders at various temperatures and times. Hydrothermal synthesis was used to prepare nanocrystalline powders of the above material with uniform crystallite size (10 nm) and chemistry. Emf measurements on the samples suggested both ionic and electronic transport, the ionic transference number decreasing with increase in the grain size. This observation was attributed to an increase in the amount of continuous crystalline grain boundary phase in the ceramics as the grain size increased. The presence of crystalline silicate and zirconate phases in the grain boundary region was confirmed by electron microscopic imaging combined with microanalysis. In the large grain (5 $\mu$m) ceramics, the ionic transference number decreased linearly with temperature. As the grain size decreased, a maximum occurred in the ionic transference number vs. temperature curve. This maximum became more pronounced at smaller grain sizes. Better grain-grain contact and the doping effect of trivalent Ce in the grain boundary core are proposed to explain this observation.

**Keywords:** electron-ion transport, $ZrO_2$-$Y_2O_3$-$CeO_2$, transference number, grain size, grain boundary phase

## Introduction

Mixed conduction of oxide ions in zirconia-yttria based ceramic systems has been a field of intense study for several years. The introduction of a multivalent cation such as Ce or Ti into the zirconia-yttria solid solution lattice is one approach followed by many investigators [1–4]. In such systems, oxygen transport can occur through the ceramic material under a gradient of oxygen pressure alone without the need for an externally applied electric field. Therefore, mixed ion-electron conductors are useful as membrane reactors in the production of high value chemicals using high temperature processes [5–7]. Their use as electrode materials in fuel cells facilitates charge transfer reactions at the electrode/electrolyte interface.

Electron jump between different valence states of the multivalent cation is the generally proposed mechanism of mixed conduction in these systems. Cales and Baumard [3] showed that in the $ZrO_2$-$Y_2O_3$-$CeO_2$ system containing up to 45 mol% $CeO_2$, a maximum in electronic conduction occurred corresponding to oxygen partial pressures at which $Ce^{3+}$ and $Ce^{4+}$ ions would exist in roughly equal amounts. This is because the probability of electron jump between these two valence states is proportional to the product of their concentrations, which is maximized when the two concentrations are equal. Swider, Loughin and Worrell [4] studied the $ZrO_2$-$Y_2O_3$-$TiO_2$ system containing up to 15 mol% $TiO_2$. Using thermoelectric measurements and electron paramagnetic resonance, they found evidence indicating the existence of extrinsic electron

*To whom all correspondence should be addressed. E-mail: changmin.chun@exxonmobil.com

[†]Present address: Department of Chemical and Biomolecular Engineering, University of Pennsylvania, Philadelphia, PA 19104, USA. E-mail: trikur@seas.upenn.edu

conduction via small polaron hopping mechanism at reduced oxygen partial pressures. Many multivalent metallic dopants, for example Ce, have a tendency to segregate to the grain boundary region when incorporated into the $ZrO_2$-$Y_2O_3$ fluorite-type lattice. One would therefore expect predominant electronic conduction along the grain boundary regions of such solid solution ceramics.

While studies in the literature cover the effect of oxygen pressure, temperature and dopant concentration on mixed conduction in selected systems, there is limited information of the role of microstructure on ionic and electronic transport behavior. There is a generally held view that the grain boundary has a blocking effect on ionic transport. Recent investigations [8, 9] have discussed grain boundary blocking effect in doped zirconia ceramics. Such blocking is suggested to be both due to the presence of siliceous impurity phases in the boundary and space charge layers adjacent to the grain boundary core. The former is termed extrinsic blocking and the latter intrinsic blocking.

The present investigation addresses the influence of microstructure on transport by selecting solid solutions of $ZrO_2$-$5.8\%Y_2O_3$-$10\%CeO_2$ as a model system. In order to correlate ionic transference number with grain size, high-density ceramic discs of various grain sizes ranging from 50 nm to 5 $\mu$m were prepared by sintering pressed powders at various temperatures and times. Nanocrystalline powders with uniform crystallite size of 10 nm and composition of $ZrO_2$-$5.8\%Y_2O_3$-$10\%CeO_2$ were hydrothermally prepared and used as the starting material. Our measurements of the electronic and ionic transference numbers in the above system do not support enhanced electronic transport along the grain boundary. Probing the grain boundary region at the nano level raises several interesting questions. In this paper, based on the microstructure of $ZrO_2$-$5.8\%Y_2O_3$-$10\%CeO_2$ ceramics having different grain sizes, hypotheses are advanced to support the observed transport behavior.

## Experimental Approach

*Hydrothermal Synthesis of Nanocrystalline Powder.*
Hydrothermal synthesis, as applied to ceramic powders and thin films, is an aqueous chemical process for the preparation of anhydrous crystalline materials in a single process [10]. It replaces high temperature calcination and mechanical milling steps required by

other chemical techniques. The ionic interactions between heterogeneous phases of both solid and solvent in hydrothermal medium determine the physical and chemical characteristics of the particles. Hydrolysis of aqueous solution of precursors with ammonia results in instant coprecipitation of ingredient ions. It should be pointed out that all of the cations are contained in the coprecipitated hydrous gel. Thus, the resultant gels possess the same composition as the precursor solution. Solid solution of $ZrO_2$-$5.8\%Y_2O_3$-$10\%CeO_2$ system was synthesized by the hydrothermal method as previously reported for $ZrO_2$ ceramics [11]. The appropriate quantities of zirconium oxy dichloride octahydrate ($ZrOCl_2 \cdot 8H_2O$, 99.9% Alfa), yttrium (III) nitrate hexahydrate [$Y(NO_3)_3 \cdot 6H_2O$, 99.9% Alfa], and Cerium (III) nitrate hexahydrate [$Ce(NO_3)_3 \cdot 6H_2O$, 99.5% Alfa] were dissolved separately in water, mixed, and coprecipitated with ammonium hydroxide at pH = 9.5. The TEM image shown in Fig. 1(a) represents the typical morphology of the gel. Selected area electron diffraction (SAED) showed a diffused ring pattern, suggesting the amorphous nature of the gel. The precipitated gels were transferred to a teflon container and hydrothermally treated at 250°C and 10 MPa for 48 hours in a steel autoclave.

It is generally accepted that the basic mechanism for the hydrothermal formation of ceramic oxide particles is dissolution-precipitation. As poorly ordered coprecipitated hydrous gel is heated in a basic aqueous medium, the solubility increases. Eventually, the solubility product of stable oxide phases is exceeded so that they begin to nucleate and grow. Figure 1(b) shows the typical morphology of the hydrothermally processed powder having an average particle size of 10 nm. The particles are generally spherical and monodispersed. The lattice fringe image shown in Fig. 1(c) confirms the crystalline nature of the particle. Also shown are Moire fringes caused by the overlapping of 1.818 Å (220) crystallographic planes. Quantitative EDXS analysis (Fig. 1(d)) reveals chemical uniformity of selected particles and confirms stoichiometry of the $ZrO_2$-$5.8\%Y_2O_3$-$10\%CeO_2$ composition. After cooling the autoclave to room temperature, the crystallized powder products were repeatedly washed with deionized water and spray dried for granulation of the particles. Atomization in spray drying generates dried particle agglomerates in the submicron range (0.25–1 $\mu$m). Uniformity of granule size is critical to the fabrication of bulk ceramic specimens while retaining nano grain size.
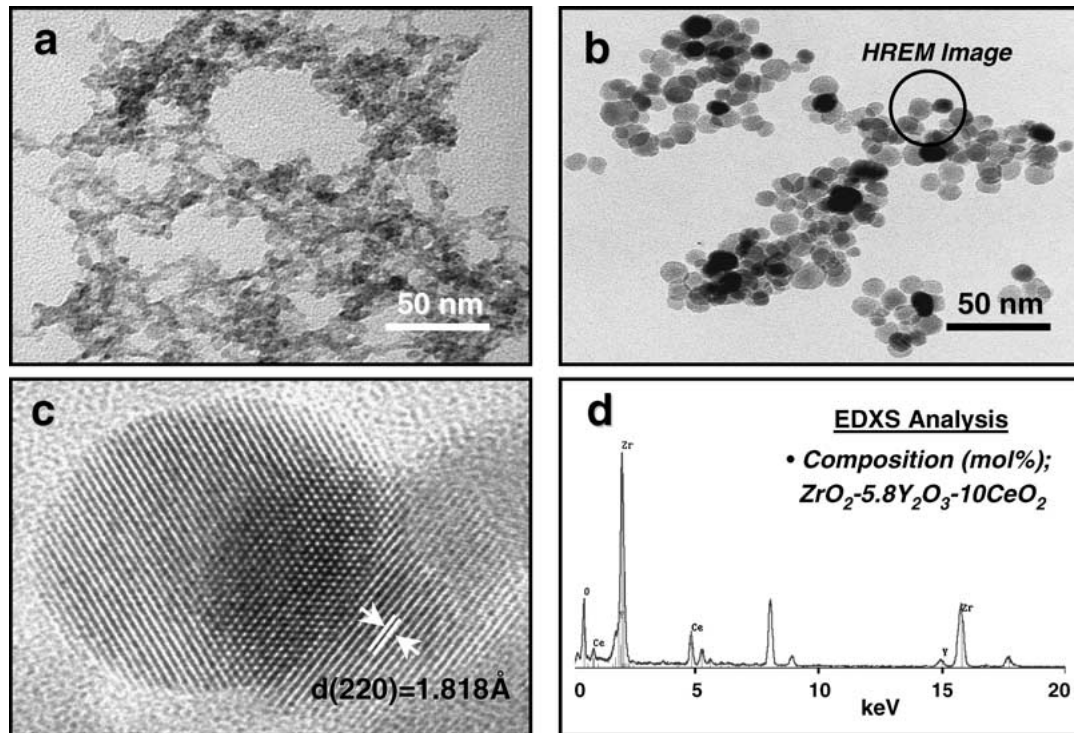
*Fig. 1*. Bright field TEM images of (a) amorphous coprecipitated hydrous gel and (b) hydrothermally prepared nanocrystalline particles of ZrO$_2$-5.8%Y$_2$O$_3$-10.0%CeO$_2$ ceramics. (c) High resolution TEM image of nanocrystalline particles showing 1.818 Å fringes of (220) lattice planes. (d) EDXS of particles revealing stoichiometric composition.

*Preparation of Dense Ceramics.* The spray-dried powder was uniaxially pressed at a pressure of 50 MPa and pre-sintered in air at a temperature of 1000°C for 2 hours to obtain disc type pellets of approximately 1 cm diameter and 1 mm thickness. A relatively fast heating and cooling rate of 20°C/min was used to suppress rapid grain growth and to retain nano-grain size. The microstructure of the rapidly pre-sintered ceramics is shown in Fig. 2(a). SEM image of the surface of ceramics sintered at 1000°C for 2 hours reveals a particulate network with open pores. In order to produce highly dense (>99%) and nano grain (grain size less than 100 nm) ceramics, hot isostatic pressing of the pre-sintered ceramics was carried out at 1100°C and 170 MPa for 4 hours. A ceramic pellet with average grain size of 50 nm was obtained (Fig. 2(b)) by this method. Samples with larger grain sizes were prepared by sintering at higher temperatures for 24 hours. The average grain sizes were 500 nm for samples sintered at 1300°C (Fig. 2(c)) and 5 $\mu$m for samples sintered at 1500°C (Fig. 2(d)). Alumina refractory lined box furnace was used for higher temper-

ature sintering in order to exclude potential impurity pick up associated with silica fiber lining. The sintered samples were over 95% of the theoretical density in all cases. The faces of all the sintered pellets were polished down to 0.1 $\mu$m finish using diamond paste.

*Microstructure Characterization.* TEM characterization of powders prepared by the hydrothermal method was carried out by dispersing the powder in methanol. After ultrasonication for 20 minutes, a few drops of the suspension were placed on a holey carbon coated TEM Cu grid, air-dried and used for characterization.

Crystal phase identification of dense ceramics was performed by Rigaku D Max II X-ray diffraction (XRD) system using monochromatic CuK$_\alpha$ radiation ($\lambda = 1.5405$ Å) with a scan rate of 0.4°/min in the 2$\theta$ range from 10° to 70°. Grain size and second phase distribution of ceramics sintered at various temperatures were investigated using a JEOL840A scanning electron microscope (SEM) before and after electrochemical transport measurements. Large grain ceramic
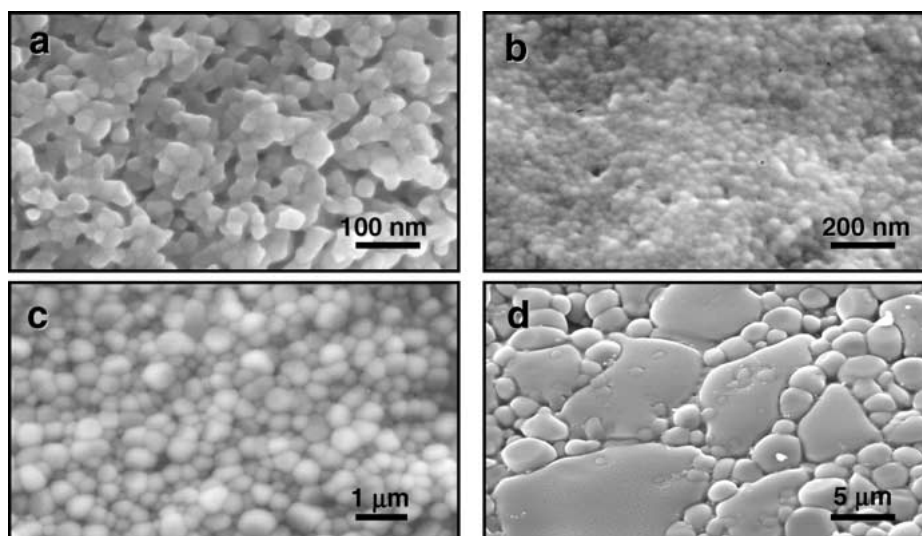
*Fig. 2.* Surface SEM images of $ZrO_2$-5.8%$Y_2O_3$-10.0%$CeO_2$ ceramics after (a) rapid pre-sintering at 1000°C for 2 hours, (b) hot isostatic pressing at 1100°C and 170 MPa for 4 hours using pre-sintered ceramics (nano grains ~50 nm), (c) sintering at 1300°C for 24 hours (fine grains ~500 nm) and (d) sintering at 1500°C for 24 hours (large grains ~5 $\mu$m).

samples were mounted in an EpoFix embedding media for cross-sectional investigation. After metallographic preparation, the distribution of grain boundary phase was examined by SEM. For both large grain and nano grain ceramic samples, high resolution transmission electron microscopy (TEM) combined with microchemical analysis was used to investigate the interface between grains at the nano level. Discs of 3 mm diameter and 100 $\mu$m thickness were cut and polished from the bulk ceramics. These were dimpled and ion-milled to generate electron transparent areas. Micrographs were taken using a Philips CM200/FEG TEM. In order to identify various elements and their approximate proportions, quantitative energy dispersive X-ray spectroscopy (EDXS) and elemental X-ray dot mapping were performed using a Princeton Gamma Tech (PGT) system attached to the TEM. A probe of approximately 5 Å in diameter was used for chemical analysis.

*Transference Number Measurements.* The ionic and electronic transference numbers were determined by open circuit measurements of the EMF developed across the ceramic using metal/metal oxide electrodes of well-defined $P_{O2}$. The metal/metal oxide electrodes were prepared in the form of disc type pellets from premixed powders. The pressed pellets of approxi-

mately 1 cm diameter and 5 mm thickness were sintered in an inert argon atmosphere. The pellet surfaces were polished to a flat finish. The mixed conductor and the metal/metal oxide pellets were assembled in a cell holder. An alumina push rod operated via a screw and spring attachment was used to exert slight pressure on the pellets to ensure excellent electrode/electrolyte interfacial contact. Platinum wires spot welded to platinum discs were used to establish electrical contact with the metal/metal oxide electrodes. A gentle flow rate of argon (50 cc/min) was maintained around the cell. The cell assembly was heated to the appropriate temperature and the Emf generated between the metal/metal oxide electrodes measured using a Hewlett Packard 3457A digital multimeter and a Solartron SR1287 electrochemical interface.

Transference number measurements by the Emf method were carried out in the temperature range, 700°C to 950°C. First, the open circuit Emf values were measured using solid electrolyte with the composition of $ZrO_2$-5.8%$Y_2O_3$.

$$Ni, NiO/ZrO_2\text{-}5.8\%Y_2O_3/Cu, Cu_2O \qquad (I)$$
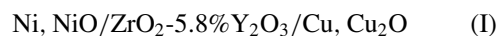
The Emf values were in good agreement with the theoretical ones derived from free energy data for $Cu_2O$

and NiO. Second, the open circuit Emf values were measured across mixed conducting ceramic discs with different grain sizes using the cell,

Ni, NiO/ZrO$_2$-5.8%Y$_2$O$_3$-10%CeO$_2$/Cu, Cu$_2$O

(II)
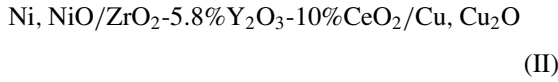
The Emf for cell (II) can be represented by the equation,

$$E = \frac{RT}{4F} \int_{P'_{O2}}^{P''_{O2}} t_{ion} \cdot d \ln P_{O2}$$

(1)

where $t_{ion}$ refers to the ionic transference number in the mixed conductor, $P''_{O2}$ represents the oxygen partial pressure of the Cu/Cu$_2$O electrode and $P'_{O2}$ that for the Ni/NiO electrode. The Faraday constant and the gas constant are represented by $F$ and $R$ respectively. If $\bar{t}_{ion}$ is used to denote the average transference number of oxide ions in the mixed conductor for $P_{O2}$ values

ranging from $P'_{O2}$ to $P''_{O2}$, then Eq. (1) reduces to

$$E = \frac{RT}{4F} \bar{t}_{ion} \ln \frac{P''_{O2}}{P'_{O2}}$$

(2)

The ratio of the Emf values of the cell II and cell I ($t_{ion} = 1$) gives an average ionic transference number value applicable for the oxygen partial pressure range covering the Cu/Cu$_2$O and the Ni/NiO electrodes.

## Results

### Nano Grain Ceramics

Figure 3(a) is a bright field TEM image, which shows the typical microstructure of nano grain ceramics having an average grain size of 50 nm. High resolution TEM image of a grain boundary shown in Fig. 3(b) indicates that no amorphous phase is present between two adjacent grains. However, EDXS analysis across
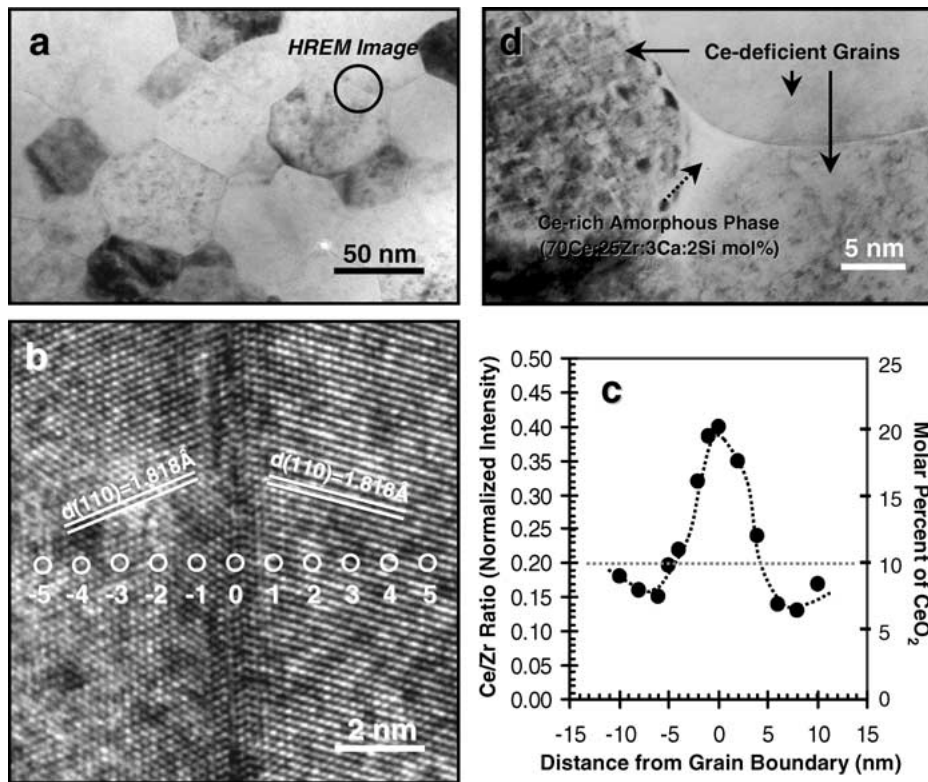


*Fig. 3.* (a) Cross sectional TEM image of nano grain ZrO$_2$-5.8%Y$_2$O$_3$-10.0%CeO$_2$ ceramics. (b) High resolution TEM image and (c) Ce distribution at every 1 nm across the grain boundary. (d) TEM image at the triple junction.

the grain boundary confirms Ce segregation over the width of $\sim$5 nm in the boundary region. The array of spots in the micrograph shows the area of EDXS analysis. Results of analysis of the Ce concentration using a 5 Å electron probe at 1 nm interval are shown in Fig. 3(c). The Ce content is seen to slightly decrease to about 7 mol% from a value of $\sim$10 mol% in the lattice and gradually increase to approximately 20 mol% at the grain boundary core. Generally, the nano grain ceramics were free of any secondary phase, but a localized cerium rich ($\sim$70 mol%) phase was observed at some triple junctions as shown in Fig. 3(d). SAED showed that the cerium rich phase was amorphous. The lateral length of the triangular pocket is about 5 nm and the dihedral angle appears to be quite small so that the amorphous phase can penetrate into the grain boundaries. However, despite the presence of local amorphous phase, no continuous amorphous films are evident at grain boundaries immediately adjacent to the triangular pocket. EDXS analysis taken from the triple grain junction revealed the chemical composition, $70CeO_2{:}25ZrO_2{:}3CaO{:}2SiO_2$ in mol%. Such second phase precipitation at triple junctions led to cerium deficiency (3.5–5.0 mol%) in the adjacent grains. Shown in Fig. 5(a) is the XRD pattern of nano size ceramics with cubic structure. No crystalline secondary phases were detected. Line broadening of cubic reflections is characteristic of the fine grain size.

*Large Grain Ceramics*

Figure 4 shows the cross sectional SEM image and X-ray map for silicon for large grain ceramics. It is seen that a secondary silicate phase is preferentially located at junctions where multiple grains meet, but a zirconate phase is also observed at the grain boundaries. A major

*Table 1.* ICP spectroscopy analysis of precursor chemicals (in ppm)

|  | Ca | Si | Na | Fe |
|---|---|---|---|---|
| $ZrOCl_2{\cdot}8H_2O$ (Alfa, 99.9%) | 0.59 | 43.8 | 0.72 | 2.80 |
| $Y(NO_3)_3{\cdot}6H_2O$ (Alfa, 99.9%) | 8660 | 56.4 | 8.04 | 0.28 |
| $Ce(NO_3)_3{\cdot}6H_2O$ (Alfa, 99.5%) | 0.59 | 5.44 | 0.59 | 0.29 |

proportion of the secondary phase observed was crystalline as confirmed by the XRD spectrum in Fig. 5(b), where silicate and zirconate phases are marked. Again, because of second phase formation in the grain boundary, the solute concentrations of adjacent grains become low enough for the zirconia ceramics to be located in the tetragonal and monoclinic phase fields. The presence of monoclinic (111) reflections and the characteristic splitting of various tetragonal peaks were observed in XRD characterization. The percentage of monoclinic phase was calculated from the X-ray intensities to be about 3%. The monoclinic phase of zirconia is usually considered unfavorable for ionic conduction.

In order to investigate the origin of secondary phase, the impurity level of precursor chemicals was determined by inductively coupled plasma (ICP) spectroscopy using Thermo Jarrell Ash IRIS plasma spectrometer. Summarized in Table 1 are the various chemical elements at ppm level. Substantial amounts of calcium ($\sim$8600 ppm) and silicon ($\sim$100 ppm) are observed. Similar ppm levels of impurities were also determined in the hydrothermally processed powder samples using the Bruker SRS3000 X-ray fluorescence (XRF) spectroscopy. Therefore, calcium and silicon originated from starting precursor materials and triggered the formation of secondary phase on sintering at 1500°C for 24 hours. In order to gain detailed information of the secondary grain boundary phases, samples of large grain ceramics were characterized by high resolution TEM.
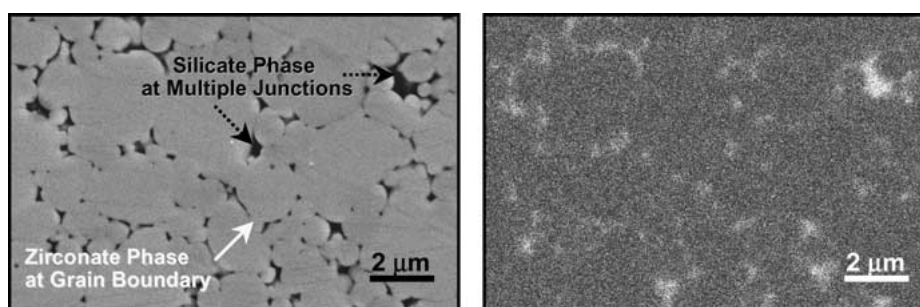


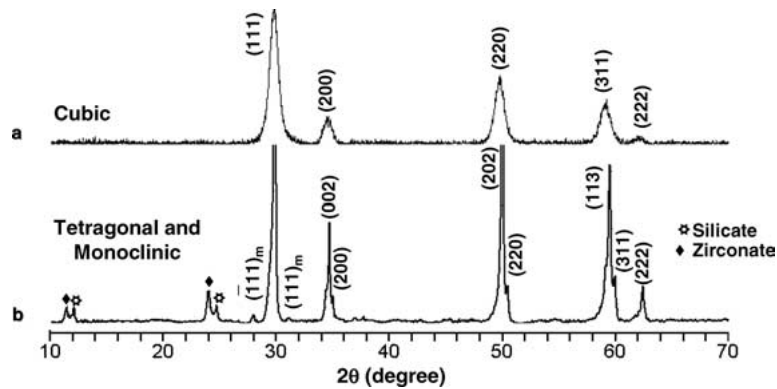*Fig. 4.* Cross sectional SEM image and combined X-ray map for Si of large grain $ZrO_2$-5.8%$Y_2O_3$-10.0%$CeO_2$ ceramics.

*Fig. 5.* XRD patterns of (a) nano grain and (b) large grain $ZrO_2$-5.8%$Y_2O_3$-10.0%$CeO_2$ ceramics.

*Grain Boundary Phases*

*Crystalline Silicate Phase.* Figure 6(a) shows a cross sectional BF TEM image and a X-ray map for zirconium of large grain size ($\sim$5 $\mu$m) ceramics. Substantial amounts of crystalline Ca-Zr-Ce silicate phase were observed at junctions where multiple grains meet. SAED pattern along the [021] zone axis orientation confirms the crystalline nature of the Ca-Zr-Ce silicate phase. Microanalysis by EDXS revealed that the chemical composition is approximately 11CaO:23$ZrO_2$:26$CeO_2$:40$SiO_2$ in mol%. Both SAED and EDXS patterns of the silicate phase are shown in Fig. 6(b). Grains adjacent to the silicate phase are Ce-deficient (<4 mol%). Also observed within the silicate phase is the yttrium rich Ce-Zr oxide phase. SAED pattern taken at the beam orientation of $B = [001]$ confirms that this oxide is fluorite type cubic phase. The corresponding EDXS analysis showed that the chemical composition of this phase is 38$Y_2O_3$:33$CeO_2$:15$ZrO_2$:6CaO:8$SiO_2$ in mol% (Fig. 6c).

*Crystalline Zirconate Phase.* Figure 7(a) shows a X-ray map for zirconium at the triple junction surrounded by three large grains. The phase within the triple junction is crystalline Ca-Zr silicate. However, compositional modulation was observed at the grain boundary, which led to the formation of Ca-Si zirconate phase. Shown in Fig. 7(b) is a bright field TEM image at the typical grain boundary of large grain ceramics. The specimen was carefully oriented so that the grain boundary was parallel to the incident beam, thus enabling the thickness of the grain boundary to

be measured. The average thickness of the continuous crystalline grain boundary phase is about 100 nm. Shown in the inset is the SAED pattern of a large tetragonal grain obtained using the beam orientation, $B = [010]$. A high resolution TEM image at the interface between a large $ZrO_2$-$Y_2O_3$-$CeO_2$ grain and Ca-Zr silicate phase is shown in Fig. 8(a). The silicate phase at the grain boundary has a composition, 20CaO:38$ZrO_2$:42$SiO_2$ in mol%, which is relatively cerium-free as shown in Fig. 7(d). Shown in Fig. 7(c) is a dark field TEM image in the same region. A triangular shaped grain at the grain boundary represents the crystalline Ca-Si zirconate phase. This image was taken after tilting the sample at [221] zone axis orientation of the Ca-Si zirconate phase and utilizing one of the diffracted electron beams as marked in the inserted SAED pattern. At the same orientation, a high resolution TEM image at the Ce-Zr silicate/Ca-Si zirconate interface was obtained (Fig. 8(b)). The Ca-Si Zirconate revealed a periodic arrangement of crystal planes. The presence of ordered superlattice domains was also confirmed by superlattice reflections in the SAED pattern. EDXS analysis revealed a chemical composition, 19CaO:11$SiO_2$:70$ZrO_2$ in mol% (Fig. 7(d)).

*Ionic Transference Number*

The ionic transference numbers for different grain sizes of $ZrO_2$-5.8%$Y_2O_3$-10%$CeO_2$ ceramics are plotted in Fig. 9 as a function of temperature. The ionic transference number is found to decrease significantly with increase in grain size. The large grain (5 $\mu$m)
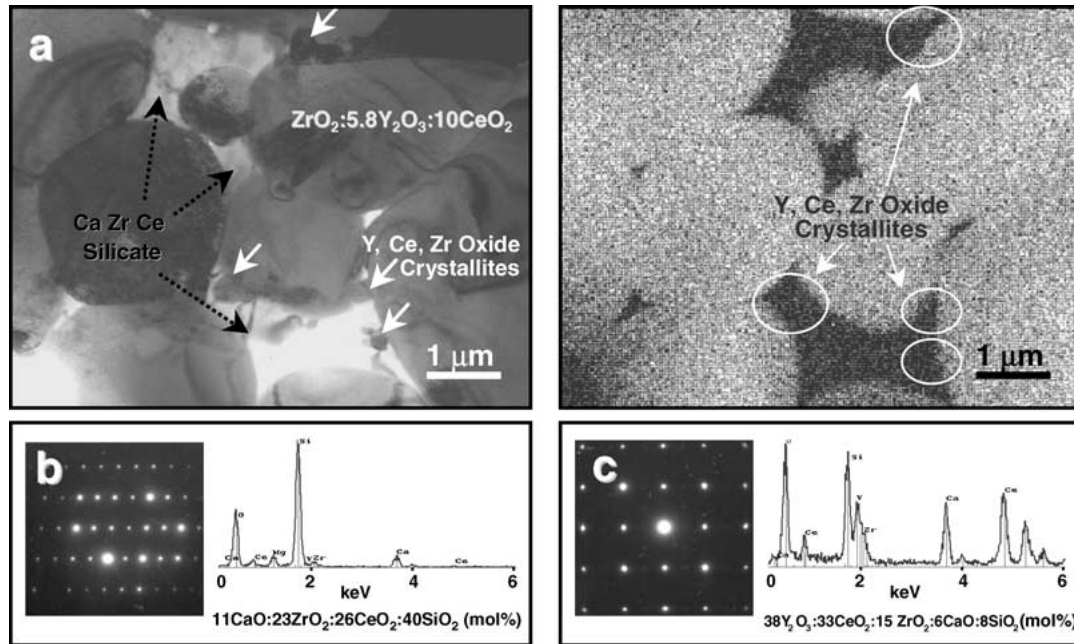
*Fig. 6.* (a) Cross sectional TEM image and X-ray map for Zr showing silicate phase at multiple junctions of large grain $ZrO_2$-5.8%$Y_2O_3$-10.0%$CeO_2$ ceramics. SAED and EDXS of (b) Ca-Zr-Ce silicate phase and (c) Y-rich Ce-Zr oxide phase.

ceramics showed very low values of the ionic transference number, which decreased linearly with temperature. For smaller-grained ceramics, the ionic transference number is found to initially increase with temperature, reach a maximum and then decrease with further increase of temperature. This maximum became more pronounced and shifted to higher temperatures for nano grain ceramics, occurring around 850°C for the 50 nm ceramics. Ramanarayanan, Ling and Anderson [12] have previously shown that under conditions of constant total conductivity and small oxygen partial pressure gradients, a maximum ionic flux is achieved at a transference number of 0.5. It is interesting to observe that for the 50 nm ceramics, a value of $t_{ion} = 0.5$ occurs at two different temperatures, 750°C and 950°C.

## Discussion

### Grain Boundary Phases in Large Grain Ceramics

The present results suggest that, even in materials without deliberately added $SiO_2$ and $CaO$, some influence of cosegregation with other dopants such as $CeO_2$ remains

present and must be accounted for in the interpretation of the segregation mechanism. The segregation of impurity elements in zirconia based ceramic systems has been studied extensively. Theunissen, Winnubst and Burggraaf [13] have reported yttrium segregation at the grain boundaries of yttria stabilized zirconia ceramics. Hwang and Chen [14] have observed segregation of calcium and other divalent and trivalent solutes to grain boundaries in tetragonal zirconia, which they attributed to space charge effects. Aoki et al. [15] have also observed cosegregation of calcium and silicon at the grain boundary in high purity stabilized zirconia. However, the secondary siliceous phase inclusions were amorphous and localized discontinuously at the grain boundary.

Our present investigation revealed the evolution of continuous crystalline secondary phases. Substantial cosegregation of calcium and silicon and their compositional modulation at the grain boundary triggered the formation of crystalline Ca-Si zirconate and Ca-Zr-silicate phases. Cerium segregation occurred preferentially at junctions where multiple grains meet, resulting in the formation of the crystalline Ca-Zr-Ce silicate phase. Significant cosegregation of various dopants initially develops a liquid phase during sintering at high
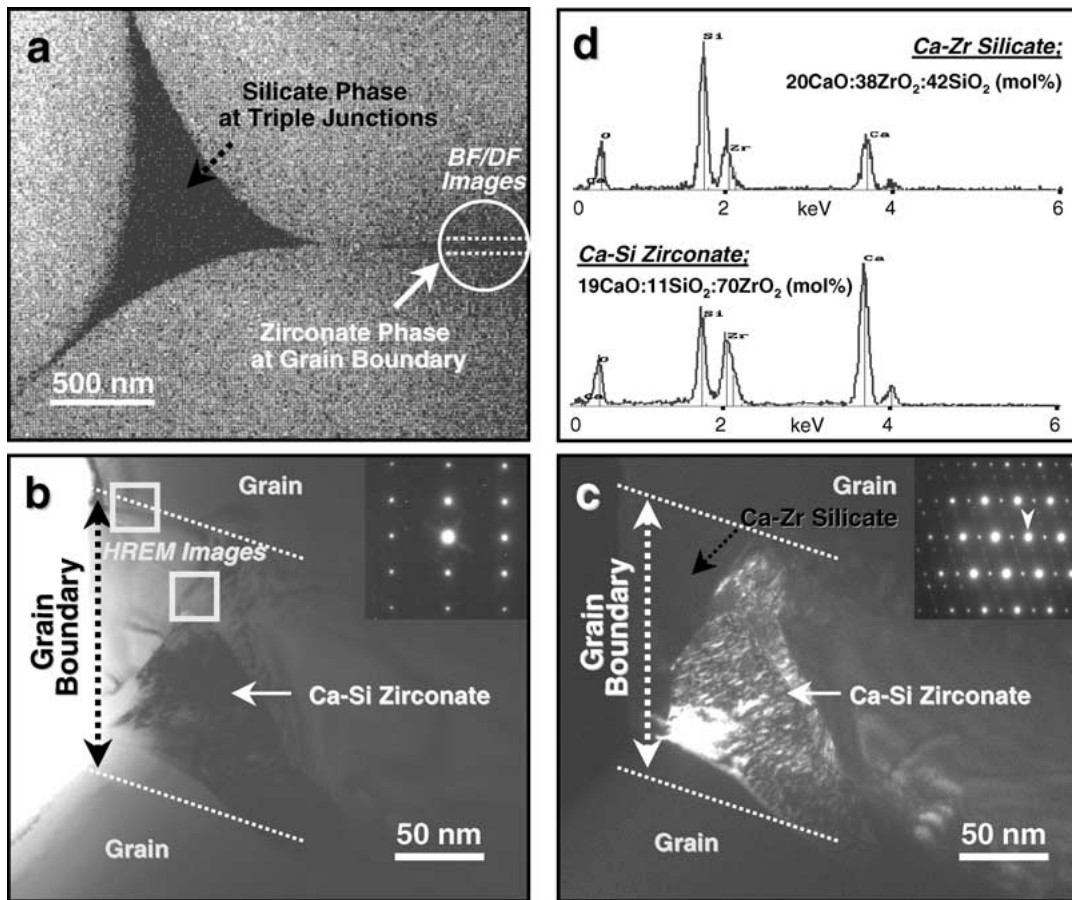
*Fig. 7.* (a) X-ray map for Zr showing silicate phase at triple junction and zirconate phase at grain boundary. (b) Bright field and (c) dark field images of Ca-Si zirconate phase at grain boundary of large grain ZrO$_2$-5.8%Y$_2$O$_3$-10.0%CeO$_2$ ceramics. (d) EDXS of Ca-Zr silicate and Ca-Si zirconate phases at grain boundary.



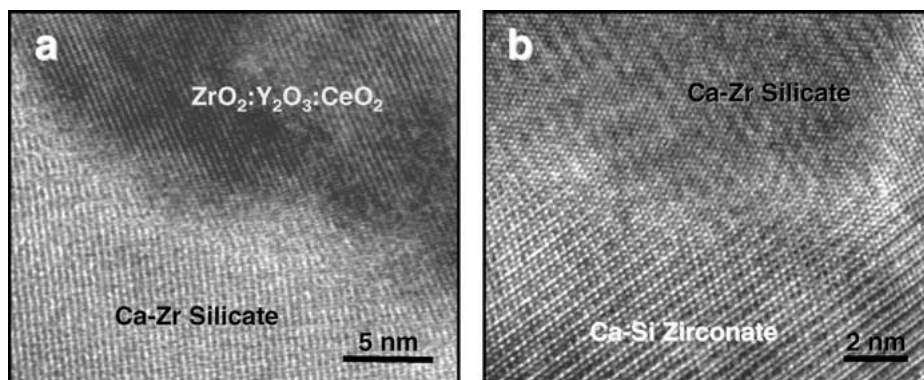*Fig. 8.* High resolution images of large grain ZrO$_2$-5.8%Y$_2$O$_3$-10.0%CeO$_2$ ceramics showing lattice fringes (a) at a large grain/Ca-Zr silicate interface and (b) at Ca-Zr silicate/Ca-Si zirconate interface.
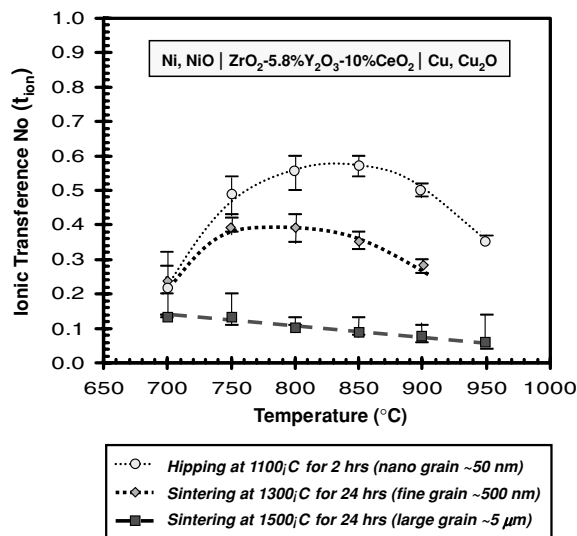
Ni, NiO | ZrO$_2$-5.8%Y$_2$O$_3$-10%CeO$_2$ | Cu, Cu$_2$O

···O··· **Hipping at 1100¡C for 2 hrs (nano grain ~50 nm)**
··◇·· **Sintering at 1300¡C for 24 hrs (fine grain ~500 nm)**
—■— **Sintering at 1500¡C for 24 hrs (large grain ~5 μm)**

*Fig. 9.* The ionic transference numbers as a function of temperatures for different grain sizes of ZrO$_2$-5.8%Y$_2$O$_3$-10%CeO$_2$ ceramics.

temperatures. On cooling, this liquid remains glassy in character which, depending on localized reactions, may not be of uniform composition throughout the ceramics. The liquid phase is relatively mobile at the sintering temperature, and as a result it tends to surround the crystalline particles and form a continuous matrix, bonding the grains and filling the interstices. The formation of crystalline silicate and zirconate phases involving the glass phase may occur spontaneously during cooling.

It is interesting to note that the presence of Ca-Zr silicate phases has been studied previously in the silicon nitride system having additives of zirconia [16]. Since calcium is commonly present as an impurity in silicon nitride, the ternary compounds are crystallized at grain boundary pockets. As possible silicate phases Ca$_3$ZrSi$_2$O$_9$ (Baghdadite), Ca$_2$ZrSi$_4$O$_{12}$ and CaZrSi$_2$O$_7$ (Gittinsite) were proposed. This study suggests that the crystalline silicate phase observed in large grain ceramics of the ZrO$_2$-5.8%Y$_2$O$_3$-10%CeO$_2$ system may be one of these silicate phases. At the same time, calcium as an impurity element can be enriched locally and may exceed 17 mol%. Since the eutectoid decomposition of the cubic solid solution occurs at 1140°C and 17 mol% CaO based on the ZrO$_2$-CaO phase diagram, CaZr$_4$O$_9$ type zirconate phase can be formed in sintered cubic solid solution [17]. The observation of Ca-Si zirconate phase at grain

boundary containing about 19 mol% CaO, supports this explanation.

### *The Effect of Microstructure on the Mixed Conduction*

In earlier investigations of the conduction properties of the ceria-doped zirconia based ceramic systems [3, 18], the hopping of electrons between cerium cations of different valences was suggested as the mechanism of electronic conduction. Substantial Ce segregation in the grain boundary region of nano grain ceramics suggests that the grain boundary may be a preferred path for electronic conduction. Therefore, the electron exchange reaction,

$$Ce_{Zr} + e' = Ce'_{Zr} \tag{3}$$
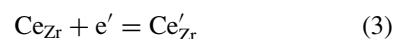
could occur predominantly in the grain boundary and be responsible for electronic conduction in this system. According to Mistler and Coble [19], the region of grain boundary transport can be much wider than the geometrical width of the grain boundary region. Wang and Kroger [20] have advanced a similar argument and have extended point defect descriptions typically used for the lattice to the grain boundary region also. This consideration makes it possible to apply reaction (3) to the grain boundary region.

For a given impurity content, there is more grain boundary coverage by second phase in large grain ceramics resulting in greater blocking of ionic conductivity in the boundary. In nano grain ceramics, a Ce-rich amorphous second phase is observed only in the triple point region: thus there is generally excellent direct grain to grain contact. Doped cerium in the trivalent state as a segregant could increase oxygen vacancy concentration in the grain boundary core with some resultant increase in the ionic conductivity. It is likely that both ionic and electronic conduction have increased, but the ionic conductivity more so, resulting in an increase in the ionic transference number. Optimum Ce segregation is probably achieved in a specific temperature regime where the ionic transference number is maximized. In nano grain ceramics the appearance of a maximum and further, a decrease in the ionic transference number as a function of the temperature, can be attributed to the dynamic nature of the grain boundary phase. As temperature increases, cerium segregation

to the grain boundary can increase the width of the region of Ce segregation at grain boundaries. These alterations could be responsible for the initial increase of ionic transference number up to the maximum. Above this temperature, the Ce-rich amorphous phase probably gets relocated and spreads to the grain boundaries. Further, at temperatures above the maximum in the ionic transference number, the grain size of the mixed conductor begins to increase. Since the viscosity of amorphous phase increases with temperature, more or less partial wetting can be established at grain boundaries accounting for the effective blocking of ionic transport. A decrease in the ionic transference number with increase of temperature, as shown by the results in Fig. 9, suggests that the microstructure of the mixed conducting ceramics, in particular the formation of a continuous secondary phase with an accompanying grain size increase, has an influence on the transport behavior.

According to Maier [21], effects of interfaces such as the grain boundary on defect chemistry and conduction can be divided into core contributions and space-charge contributions. If the core is positively charged, then the concentration of all positively charged defects is depressed in the space charge region, the reverse is true for a negatively charged core. It is suggested that in the nanoceramics of the present investigation, the core contribution dominates. Because of significant cerium segregation in the grain boundary without the formation of a second phase, a high concentration of oxygen vacancies with positive effective charge are generated in the boundary core. Investigations by Chiang et al. [22] indicate that the enthalpy of reduction of oxygen leading to the formation of oxygen vacancies is significantly reduced in the grain boundary region in nano-crystalline CeO$_2$, thus facilitating the formation of V$_\mathrm{O}^{\bullet\bullet}$ defects in the core. It is suggested that optimum oxygen vacancy concentration in the grain boundary core is achieved in the present study at temperatures in the 800–825°C range. Above this temperature, the generation of second phases in the grain boundary exerts a pronounced grain boundary blocking effect to ionic transport.

TEM investigation of large grain ceramics revealed a very high coverage of grain boundaries by silicate and zirconate phases, which blocks the ionic transport by closing the conduction path. The general assumptions that secondary impurity phases have low conductivity and provide effective grain boundary blocking explain the lower oxide ion transference numbers indicated by the straight line in Fig. 9. However, total conductivity measurements are needed to gain a better understanding of transference data.

## Summary

Electrochemical transport measurements were carried out in ZrO$_2$-5.8%Y$_2$O$_3$-10%CeO$_2$ ceramic system as a function of temperature and grain size. The grain size was varied from 50 nm to 5 $\mu$m. The nano grain ceramics were synthesized using a hydrothermal technique. The ionic transference numbers, measured in the temperature range, 750–950°C, decreased with grain size. In the 5 $\mu$m ceramics, which exhibited the lowest ionic transport, the ionic transport number decreased linearly with temperature. With decrease in grain size, there was an increase in ionic transference. Furthermore, the shape of the ionic transference number vs. temperature curve changed, exhibiting a pronounced maximum around 850°C for the 50 nm ceramics.

The above observation can be explained on the basis of segregation phenomena in this ceramic system as a function of grain size and temperature. In the 5 $\mu$m ceramics, a continuous crystalline Ca-Zr-Ce silicate phase was observed at junctions where multiple grains meet and a Ca-Si zirconate phase of about 100 nm thickness was present in the grain boundary region. Grain-grain contact was thus significantly restricted by the presence of these grain boundary phases, which thus served to block ion transport. In the nano grain ceramics, on the other hand, a discrete Ce-rich phase was found only at the triple junctions. There was significant grain boundary segregation of Ce ($\sim$20 mol%) without the precipitation of a second phase. Thus, there was excellent grain-grain contact, which prevented blockage of ion transport. Furthermore, the trivalent part of the segregated Ce can be expected to increase the oxygen vacancy population in the grain boundary core by doping, leading to a further increase in ionic transport. It is likely that with increase in temperature, grain boundary segregation of Ce increases, leading to an increase in the ionic transference number. Beyond the maximum, which occurred around 850°C, it is suggested that the segregation pattern changed and a second phase indeed started to wet the grain boundary, contributing to a decrease in the ionic transference number. Total conductivity measurements are needed to further explain the observed behavior.

## References

1. E.A. Hazbun, US Patent No. 4,791,079 (1988).
2. K.W. Browall and R.H. Doremus, *J. Am. Ceram. Soc.*, **60**, 262 (1977).
3. B. Cales and J.F. Baumard, *J. Electrochem. Soc.*, **131**, 2407 (1984).
4. K.E. Swider, S. Loughin, and W.L. Worrell, in *Proc. First Int. Symp. Ionic and Mixed Conducting Ceramic*s, edited by T.A. Ramanarayanan and H.L. Tuller (The Electrochemical Society, Pennington, NJ, 1991), p. 73.
5. E.A. Hazbun, US Patent No. 4,827,071 (1989).
6. T.L. Cable, J.G. Frye, Jr., and T.J. Mazanec, Eur. Pat. No. 399833A1 (1990).
7. T.J. Mazanec, *Solid State Ionics*, **70/71**, 11 (1994).
8. X. Guo and J. Maier, *J. Electrochem. Soc.*, **148**, E121 (2001).
9. X. Guo, W. Sigle, J. Fleig, and J. Maier, *Solid State Ionics*, **154/155**, 555 (2002).
10. W.J. Dawson, *Ceramic Bulletin*, **67**, 1673 (1988).
11. E. Tani, M. Yoshimura, and S. Somiya, *J. Am. Ceram. Soc.*, **66**, 11 (1983).
12. T.A. Ramanarayanan, S. Ling, and M.P. Anderson, in *Proc. First Int. Symp. Ionic and Mixed Cond. Ceramics*, edited by T.A. Ramanarayanan and H.L. Tuller (The Electrochemcial Society, Pennington, NJ, 1991), p. 110.
13. G.S.A.M. Theunissen, A.J.A. Winnubst, and A.J. Burggraaf, *J. Mater. Sci.*, **27**, 5057 (1992).
14. S.L. Hwang and I.W. Chen, *J. Am. Ceram. Soc.*, **73**, 3269 (1990).
15. M. Aoki, Y.M. Chiang, I. Kosacki, L.J. Lee, H. Tuller, and U. Liu, *J. Am. Ceram. Soc.*, **79**, 1169 (1996).
16. P.E.D. Morgan, J.L. Kicks, J.A. Bump, and M.S. Koutsoutis, *J. Mater. Sci. Lett.*, **6**, 559 (1987).
17. V.S. Stibican, in *Advances in Ceramics*, Vol. 24A, edited by S. Somiya, N. Uamamoto, and H. Yanagida (The American Ceramic Society, Westerville, OH, 1988), p. 71.
18. T.A. Ramanarayanan, L. Ling, J.D. Mumford, A. Ozekcin, and V.K. Pareek, *Solid State Ionics*, **94**, 259 (1997).
19. R.E. Mistler and R.L. Coble, *J. Appl. Phys.*, **45**, 1507 (1974).
20. H.A. Wang and F.A. Kroger, *J. Am. Ceram. Soc.*, **63**, 613 (1980).
21. J. Maier, *Solid State Ionics*, **148**, 367 (2002).
22. Y.-M. Chiang, E.B. Lavik, I. Kosacki, and H.L. Tuller, *J. Electroceramics*, **1**, 7 (1997).